

Effects of polymer infiltration processing (PIP) temperature on the mechanical and thermal properties of Nextel 312 Fibre SiOC ceramic matrix composites

Accepted Nov 2020: Composites Part A: Applied Science and Manufacturing

Talha J. Pirzada¹, Shraddha Singh, Robin De Meyere, Philip Earp, Marina Galano, T. James Marrow

Department of Materials, University of Oxford, Parks Rd, Oxford, OX1 3PH, UK

Highlights:

- Porosity increased, and density decreased, with increased PIP temperature
- The lowest PIP temperature (850°C) gave the weakest fibre-matrix interface
- The highest PIP temperature (1050°C) gave the best thermo-gravimetric stability
- The effective flexural modulus decreased with increasing tensile strain

Abstract

Effects of the polymer infiltration processing (PIP) temperature between 850 and 1050°C on the mechanical and thermal properties of Nextel 312 fibre SiOC ceramic matrix composite were studied. The aim was to optimise the material system for its proposed application as a mechanical gas-seal at temperatures up to 900°C. The microstructure and its failure behaviour at room temperature were characterised using

¹ Corresponding author. talha.pirzada@linacre.ox.ac.uk

20 electron microscopy (SEM, TEM), X-ray diffraction and high resolution X-ray
21 Tomography, with mechanical testing by nano-indentation, fibre-push out and flexural
22 bending. Thermo-gravimetric analysis quantified the thermal stability. Processing at
23 950°C or above gave a combination of high effective elastic modulus, good resistance
24 to mechanical damage from tensile strain and good thermal stability.

25 **Keywords:** A. Ceramic-matrix composites (CMCs); B. Fracture; D. Thermal analysis;
26 D. Mechanical testing

27

28

29

30

31

1 Introduction

Materials for high temperature gas seals in aerospace components, such as engines and rockets, have received attention in recent years due to the need for reduced weight and higher operating temperatures for increased efficiency [1–3]. In order to mechanically seal a gap, the sealant must possess three characteristics. Firstly, it should have sufficient compressibility to accommodate additional strains caused by thermal expansion of the surrounding parts. Secondly, it should have sufficient elastic ‘spring’ retention at the operating temperature to maintain the gap closure. Thirdly, the material must be sufficiently impermeable to prevent gas outflow to realize an effective gas seal. In current aero-engines, the gas seal is achieved using metallic alloys (such as Inconel 718), which have a maximum operating temperature of 750°C [4].

Ceramic matrix composites (CMC) are excellent candidates for high temperature applications due to their inherent oxidation resistance and good thermal shock resistance [1, 5]. They can also have high toughness by encouraging quasi-ductile deformation as toughening mechanisms such as crack deflection, fibre pull-out, crack bridging and debonding are achieved through optimal control of the interface between fibre and matrix [6, 7]. Lower interfacial shear strength between the fibre and the matrix can maximise crack deflection and increase fracture resistance to provide flaw insensitivity and damage tolerant behaviour [1]. To design CMCs for critical high-temperature aerospace applications such as seals, the three main material components (i.e. fibre, the matrix and the interface) must be selected and controlled to obtain the required performance; that is to (a) maximise the range of elastic deformation in the component; (b) minimise stress relaxation at service temperature; and (c) have a fibre/matrix interface that is chemically stable at the service temperatures [8, 9]. Oxide-based

ceramic matrix composites are stable in oxidising atmospheres such as combustion gases, and aluminosilicate fibre/mullite matrix composites with a porous matrix exhibit damage tolerant behaviour up to 1200°C [10–12]. The infiltration-processed mullite matrix retains strength at 1200°C while providing oxidation stability [13,14], and techniques such as electrophoretic infiltration can also be used to deposit the matrix onto the fibres [15].

To satisfy seal design requirements at high temperature, an oxide based ceramic matrix composite (OxCMC) has been proposed that is composed of Nextel 312 fibre with a SiCO matrix. Nextel 312 is a commercially available polycrystalline metal oxide ceramic fiber, with a composition of 62% Al_2O_3 , 24% SiO_2 , and 14% B_2O_3 (percentage by weight) [16]. Nextel 312 has a fibre diameter of about 10 μm , density of 2.8 g/cc, a coefficient of thermal expansion of about 3 ppm/°C [16], and retains its strength at 900°C for extended periods [12]. The SiCO matrix, known as ‘Blackglas’, has a chemical composition of 42 wt. % Si, 20 wt. % C, and 38 wt. % O_2 . The fibres have a boron nitride (BN) coating, which is obtained by their exposure to an ammonia atmosphere at high temperature [17].

Previous work on optimising the manufacturing parameters to produce a Nextel 312/SiCO composite for high temperature applications[18,19] showed it could be net-shape fabricated with the matrix in a glassy state. The processing first converts the matrix, a mixture of polysiloxane monomers, by heating in the presence of a hydrosilylation catalyst to produce a cross-linked thermoset polymer. This is then pyrolyzed to develop the oxide matrix. Both pyrolysis temperature and atmosphere are important factors in processing. Pyrolysis at 1100°C has been shown to produce a more oxidatively stable sample in comparison to pyrolysis at 900°C [20,21]. In a study of the

oxidation behaviour at 1000°C of Nextel 312/SiCO samples, pyrolyzed at different temperatures and in different atmospheres (ammonia and argon) [22], it was demonstrated that the argon pyrolyzed composite lost more weight due to decomposition of the pyrolytic carbon, whereas the ammonia pyrolyzed composites were stable as both the N and C were bonded to Si in the matrix. Samples pyrolyzed in ammonia also contained higher porosity than those pyrolyzed in argon.

Tensile tests of Nextel 312/SiCO composites [23] at room temperature and 760°C found no significant change in failure strength over this range. The average failure strains, with tensile strength of ~65 MPa, at room temperature and elevated temperature, were 0.13% and 0.25% respectively. This increase was attributed to residual stresses in the composite that develop after processing during the cooling down phase. As the elevated test temperature of 760°C was close to the PIP temperature, the composite was mostly stress free. Post-mortem analysis suggested that the damage initiated from macro-pores present in the warp and weft yarn. This was followed by matrix cracking, interfacial debonding and fibre cracking.

The BN coating of the fibres can be affected by the operating environment. After 100 hrs of exposure at 600°C, the strength and strain bearing capabilities of a Nextel 312/SiCO were reduced due to fibre interface oxidation [22,24]. In a comparative study [25], composites with either Nicalon or Nextel 312 fibres in a SiCO matrix were manufactured using vacuum assisted resin transfer moulding, with and without an applied injection pressure. The SiC-based Nicalon fibres had a carbon coating, whereas the Nextel 312 fibre were BN coated. Samples produced without injection pressure had higher density and fibre volume fraction, and exhibited higher strength and displacement to failure. After high temperature exposure at 800°C in air, the Nicalon

composite had lower strength and displacement to failure in comparison to the Nextel 312 composite, as the BN coating was more stable at higher temperatures.

This paper is part of work to optimise Nextel 312/SiCO composites for sealing applications at service temperatures up to 900°C, using repeated matrix impregnation and pyrolysis (polymer infiltration processing, PIP). The effects of the polymer infiltration temperature on the mechanical, morphological and thermal properties have been studied. The microstructures were analysed using SEM, TEM, XRD and X-ray computed tomography in order to quantify the differences arising from the manufacturing process. The materials were tested mechanically to determine their strength, ductility and fracture behaviour. Nano indentation quantified the elastic modulus and hardness of the fibre and the matrix, and micro-mechanical fibre pushout tests measured the interfacial shear strength. The thermal stability of the composites was investigated using thermo-gravimetric analysis (TGA). The objective was to identify the PIP temperature that could provide the optimum combination of properties of high elastic flexural deflection, thermal stability, low interfacial shear stress for toughening and low mass loss up to the intended service temperature. Future studies will examine the gas permeability of these material systems, and the effects of mechanical damage on this.

2 Materials and Methods

2.1 Material Processing

The manufactured composites were composed of Nextel 312 fibre, woven in a harness satin weave structure, with SiCO matrix and a boron nitride interface. The fibre coating of BN was achieved by diffusing boron, from the boria (B_2O_3) that inherent within

Nextel 312, to the fibre surface by heating the fibres in an ammonia atmosphere at temperature above 1000°C. A pre-ceramic slurry of polycarbosiloxane, with highly doped silicon carbide sub-micron particulates as filler material, was then impregnated into the fabric to create a prepreg. The prepreg fabric was laid out in a 0°/90° composite stack and autoclave cured at 825 kPa and a temperature between 150-200°C for 240 minutes. All processing was done in an argon atmosphere.

Pyrolysis, to convert the green-state polymer into a silicon oxi-carbide matrix by thermal transition of the polycarbosiloxane, was carried out at temperatures between 850°C and 1050°C under protection of an argon atmosphere. Each cycle of reimpregnation of the porous matrix was carried out in vacuum (75 kPa) and ambient temperature. In addition to the initial pyrolysis, each material was subjected to five additional infiltration-densification cycles (Table 1) to produce four sample materials for testing and characterisation.

2.2 Microstructure Characterisation

Scanning electron microscopy was carried out using a Merlin Field Emission microscope (Carl Zeiss SMT AG), equipped with an Xmax 150 EDX detector for elemental mapping and analysis. The samples were prepared by mounting in conductive epoxy resin and polishing with 1200 grit SiC paper, then 6 µm, 3 µm, and 1 µm diamond paste to finish with colloidal silica. This was followed by ion beam polishing using a PIPS II system, then coating with carbon by a Q150R Plus plasma rotary pump sputter coater. Transmission electron microscopy was carried out using a JEOL 2100 TEM, with the sample prepared by thinning a 3 mm disk (cut using a precision saw and

ultrasonic cutter) to 50 μm using manual polishing followed by ion beam milling to perforation with a Gatan 691 precision ion polishing system.

The microstructures were examined by computed tomography with an Xradia Versa 510 X-ray microscope, operated at 80 kV energy, and 7 W power. The analysed specimens were 15 mm long with a cross-section of 4 x 5 mm. Each tomograph was reconstructed from 2000 projections recorded over a 360° rotation about the specimen's longest axis, with 2x binning of the 2048 x 2048 pixel camera, to obtain an image volume with a voxel size of 3.1 x 3.1 x 3.1 μm . The tomographs were reconstructed (16-bit greyscale) using the Xradia software. The Avizo 9.5 image visualization software was used to quantify the observed porosity, using segmentation by greyscale thresholding.

X-ray diffraction (XRD) analysis was carried out on powdered specimens using a Bruker D8 ADVANCE eco powder diffractometer employing copper K_{α} radiation ($\lambda=0.15406$ nm) and a LYNXEYE XE detector. Each specimen was continuously spun during data collection and scanned using a step size of 0.02° (2 θ) over the range of 10°-80° (2 θ) at $\sim 0.5^{\circ} \text{ min}^{-1}$, with the baseline subtracted from the raw data to define the characteristic peaks.

Thermo-gravimetric analysis was carried out in an open alumina pan under a constant flow of air at 20 ml min^{-1} using a Perkin Elmer Pyris 1 TG/DTA instrument. The specimens were each approximately 15 mg of material (measurement precision 0.005 mg) and were heated from 30°C to 975°C at a rate of 3°C min^{-1} . The bulk density for each material was obtained by measurement of the mass (precision of 1 mg) and external dimensions (precision of 0.01 mm) of rectangular specimens. The open porosity was measured in a sample 1 (850°C PIP): after measuring the dry weight, the sample was submerged in a brine solution (specific gravity 1.1999) under a pressure of

0.8 bar for 5 minutes; and on removal, the excess solution was dried with a paper towel and the saturated sample was re-weighed to determine the mass of the absorbed solution and hence the volume of the open pores.

2.3 Mechanical Testing

Three-point flexural bend tests were done using a Shimadzu universal testing frame with a 5 kN load cell. Each specimen was tested in the 0°/90° ply orientation with the 0° fibres aligned in the longitudinal direction. The specimen thickness and width were nominally 5 mm and 4 mm, measured to ± 0.01 mm. The span was 60 mm with loading and supporting pin diameters of 4 mm. A displacement rate of 0.1 mm min^{-1} was used. Three specimens from each sample material were tested.

A single camera optical system was used to observe the specimens during the bend tests, with an image pixel size of $6 \text{ }\mu\text{m}$ and a $15 \times 18 \text{ mm}$ field of view centred on the central loading pin. Each specimen was prepared by first coating the surface with Hycote matt white paint, which was then sprayed with a very fine speckle pattern of acrylic black ink, diluted with acetone, applied with an airbrush from a distance of 50 cm to achieve an average speckle size around $1\text{-}10 \text{ }\mu\text{m}$. The images, recorded at a frequency of 1 Hz, were processed with the LaVision Davis 8.3.1 Digital Image Correlation software using the Least Square and time series approximation methods. A final subset size of 40 pixels was selected along with a step size of 5.

2.4 Micromechanical Testing

Nano-indentations were performed using a Berkovich tip on a Nano-indenter XP (Agilent Technologies, USA). The specimens were polished to sub-micron level using

diamond polishing media followed by colloidal silica, then ultra-sonicated in an acetone bath for 10 minutes before attachment to an aluminium stub with CrystalbondTM adhesive. A nano-indenter penetration depth of 800 nm was selected for the matrix, and a penetration depth of 200 nm was selected for the fibres due to their smaller dimension. An average of 40 indents were made in both fibres and matrix for each material.

Specimens for fibre pushout tests were ground to an average thickness of around 100 μm (maximum thickness 300 μm), polished on both sides to sub-micron level using diamond polishing media followed by colloidal silica and then ultra-sonicated in an acetone bath (10 minutes) followed by two ethanol baths (5 minutes each) to remove surface wax that had been used to fix the specimens during polishing. The specimens were then attached with minimal amount of wax to a holder [26] that was designed to enable pushout without bending of the test specimen. The pushout tests used a NanoG200 nano-indentation instrument, equipped with a 40x objective lens and a 5 μm radius flat-tip punch that could achieve a maximum pushout displacement of 6 μm . SEM images were recorded before and after set of pushout tests to identify the successful pushouts. Measurements of the specimen cross-sectional thickness, fibre diameters and pushout lengths were also obtained by SEM.

3 Results

3.1 Microstructure Characterisation

Figure 1 presents SEM images of the overall structure of the material, and shows the 0° and 90° fibre tows within the matrix. The microstructures of all four samples are indistinguishable, hence only example images for sample 1 are shown. Matrix defects (pores with a size of around 200 μm) are observed (Figure 1a). The fibres bundles are

embedded in the matrix, which tends to be cracked orthogonally to the fibre layers.

Individual fibres have an elliptical cross-section, oriented at various angles within the fibre bundles (Figure 1b). TEM imaging (Figure 1c) reveals the 30-40 nm thick BN interface between the matrix and the fibre. The matrix also contains nano-particles, similar in appearance to those identified in the literature as SiC [16], as expected from the processing.

The XRD data (Figure 2) from the four samples are indistinguishable, with any differences in the crystalline structure below the resolution of this technique. Their crystalline content is predominantly boron-mullite ($\text{Al}_9\text{BSi}_2\text{O}_{19}$), with smaller contributions from silicon carbide (SiC), and aluminium boron oxide ($\text{Al}_4\text{B}_2\text{O}_9$). The boron-mullite and the aluminium boron oxide are the expected crystalline phases in these fibers, and the matrix has been reported as amorphous and containing crystalline SiC [16].

X-ray tomography (Figure 3) shows the three-dimensional arrangement of the fibres and matrix, and clearly shows the distribution of the matrix cracks that are significant contributors to the internal porosity of the material. An orthoslice of the tomograph reveals the cracks and micropores in more detail (Figure 3a). The porosity measurements obtained by threshold segmentation of the μXCT images (Table 2) show the total amount of porosity increased with PIP temperature from ~9% at 850°C PIP to ~15% at higher temperatures; the porosities of samples 3 and 4 are indistinguishable. The uncertainty in the porosity was estimated as the sample standard deviation of 5 measurements at different non-overlapping locations for each sample, each with volume ~27 mm³. A sensitivity study determined the optimum segmentation threshold to quantify the observable porosity and to estimate the measurement error (SEE

SUPPLEMENTARY INFORMATION). The bulk density measurements (Table 2), showed a similar decrease in density with increase in PIP temperature from a specific gravity of 2.4 ± 0.2 in sample 1 (850°C PIP) to 2.2 ± 0.2 in samples 3 and 4. For the highest density material, processed by PIP at 850°C, the brine penetration measured an open pore volume of $8.33 \pm 1.18 \text{ mm}^3$ for a sample with dimensions of $19.35 \times 4.01 \times 4.99 \text{ mm}$. The open porosity of $2.15 \pm 0.30 \%$ is approximately 20% of the total porosity observed by μXCT . This indicates that the majority of the porosity is closed, which is beneficial for low gas permeability.

Example traces of the relative mass change in the TGA from 25°C to 975°C are shown in Figure 4. They show a two-step weight loss process. The data, summarised in Table 3, report the total mass change (%) and the changes within intervals up to 300°C; between 300 and 600°C; and between 600 and 900°C. Sample 1, with the lowest PIP temperature, show the greatest mass loss (6.5% total), whereas samples 2 to 4 are similar at 4 to 4.5%. The most significant weight loss occurred above 600°C.

3.2 Mechanical Testing

Figure 5 shows the nominal (i.e. effective) flexural stress vs flexural strain curves from the tests of three specimens of each sample. The effective strains and stresses were calculated using the cross-head displacements and simple Euler–Bernoulli beam theory, which assumes constant, homogeneous and isotropic elastic properties. For clarity, unless otherwise stated, the stresses, strains, stiffness and elastic moduli referred to in this work are effective values that are derived with this assumption. The flexural strength (i.e. maximum flexural stress) and flexural moduli, obtained using a linear fit between 0.1 and 0.2% strain, are summarised in Table 4. All specimens showed similar

stiffness, with some non-linearity at high strain. The largest strains to failure were observed for specimens from sample 1.

Examples of the surface strain fields obtained by the DIC analysis are presented in Figure 6 using the maximum normal 3D strain (i.e. displacement gradient), which is sensitive to discontinuities of the displacement field that are caused by cracks [27–30].

This finds no evidence of cracking up to 0.9σ (i.e. 90% of σ , the flexural strength that is the flexural stress at maximum load). At the flexural strength, cracks are observed to propagate from the tensile surface in all samples. The fracture tends to be deflected parallel to the lamination of the microstructure, particularly in sample 1.

The load-line displacements were estimated by DIC measurement of the vertical movement of the specimen underneath the load pin (the support pins were not imaged and were assumed to be rigid), with an uncertainty obtained using the sample standard deviation of 5 displacement vectors within 0.12 mm of the pin. This load-line deflection, d , was then used to calculate an effective flexural modulus $E_{flexural}$ using equation (1),

$$E_{flexural} = L^3 F / 4wh^3 d \quad (1)$$

where L is the span length, F is the maximum load applied, w and h are the width and height of the specimen, and d is the load-line deflection at maximum load.

The DIC-measured displacement fields also allowed the effective flexural modulus of the specimens to be quantified via the sample curvature. This was done by measuring the relative differences in x -displacement between points on two vertical (y) plane, positioned on either side of the central loading pin and separated by a gauge distance of 10 mm (Figure 7); in this region, the bending moment is within 5% of its maximum

value. The average strain ϵ_x in this region was therefore obtained as a function of position, y . Euler–Bernoulli beam theory was then used to estimate the effective elastic modulus. The analysis assumed no movement of the neutral axis, and used the linear gradient of the strain, $\frac{d\epsilon_x}{dy}$, to estimate the beam’s radius of curvature, r , thus [31]:

$$M = E_{eff}I/r \text{ where } \frac{d\epsilon_x}{dy} = -1/r \quad (2)$$

where M is the bending moment, I is the second moment of area of the beam, and E_{eff} is the effective elastic modulus.

The normalized flexural strains ϵ_x/M as a function of distance from the beam centre for load are shown in Figure 8. For sample 1, which had the lowest PIP temperature, there is a clear increase in the gradient with increasing load, which indicates a reduction in effective flexural modulus, together with a shift in the position of the neutral axis by ~0.5 mm towards the tensile surface. Similar, but smaller, reductions in modulus are observed at high load in the other samples. The effective flexural moduli, obtained via the load-line deflection (equation 1) and the specimen curvature (equation 2, fitted via linear regression), are presented in Figure 9a and b. The load-line moduli decrease with increasing load for samples 1, 2, and 4, and are practically constant for sample 3 that had the highest modulus. The moduli measured via the strain gradient all decrease with increasing load; sample 3 has the highest modulus. The moduli obtained at 20 N (~18 MPa) and 60 N (~54 MPa) using both strain gradient and load-line displacement are summarised in Table 4. The strain gradient moduli, relative to that obtained at 20 N, are presented in Figure 9c as a function of flexural strain (calculated using the load-line displacement). All samples show a relative decrease in effective flexural modulus with

increasing strain; samples 3 and 4 are least affected and maintain similar and higher relative moduli than samples 1 and 2 to a strain of at least 0.1%.

3.3 Micromechanical Testing

The nano-indentation data (Figure 10), after rejecting those indents that did not fully sample matrix or fibre, show the four samples have a fibre modulus of ~120 to 140 GPa and hardness of ~10 GPa, while the matrix modulus was ~100 to 115 GPa with a hardness 6 to 7 GPa. The uncertainties are the 95% confidence intervals of the mean (Table 5). ANOVA analysis ($p=0.05$) concludes the differences in the means for both modulus and hardness are statistically significant, with the exception of the matrix hardness for samples 1 to 3; these have means that are not significantly different from each other and are higher (~20%) than sample 4. There is no clear trend in the modulus data for fibre or matrix and though statistically significant the differences between sample means are small (<16% for both). There appears to be a weak trend for decreasing fibre hardness with increasing PIP temperature (<7% change).

The fibre pushout tests were analysed to calculate the interfacial shear stress for pushout, τ_{is} , using equation (3) [32],

$$\tau_{is} = \frac{F}{2\pi RH} \quad (3)$$

where F is the push-out load, R is the fibre radius and H is the sample thickness.

The distributions of strengths measured in successful tests are reported in Figure 11 and summarised in Table 6. Sample 1 has the lowest interfacial shear strength, with an average that is approximately half that of samples 2 to 4. The shear strength distributions, which have similar ranges in samples 2 to 4, were compared using the

unequal variances (Welch) t-test: the means of samples 3 and 4 are statistically indistinguishable ($p=0.98$); the mean of sample 2 is approximately 25% higher than 3 and 4 with statistical significance ($p<0.05$).

4 Discussion

All the samples have visually similar microstructures (Figure 1), with a proportion of defects (cracks and porosity) that increased with PIP temperature (Figure 3, Table 2). Samples 3 and 4, which had the same and highest PIP temperature in their final stage, has very similar total porosity. This is consistent with the differences in coefficients of thermal expansion of the Nextel fibre ($3 \text{ ppm } ^\circ\text{C}^{-1}$ [22]) and aluminosilicate matrix ($3.4 \text{ ppm } ^\circ\text{C}^{-1}$ [33]). These cause tensile thermal strains due to post-processing shrinkage that would be relaxed by matrix cracking. No differences in the constituent phases of the microstructure were measurable by XRD, though this technique has limited resolution [34]. There are differences between the fibre and matrix properties of the samples, measured by nanoindentation, but these are small and do not show clear trends (Table 5, Figure 10). The most significant difference due to processing is observed in the matrix of sample 4 (5 cycles at 950°C and one at 1050°C) that is $\sim 20\%$ softer than the other samples, which have the same matrix hardness.

Increasing the PIP temperature increased the thermal stability, measured as the mass loss in TGA (Figure 4 and Table 3) with sample 1, processed at 850°C , being the least stable. Sample 4 (5 cycles at 950°C and one at 1050°C) has the highest thermal stability, though the behaviour of samples 2 to 4 is quite similar. The two-stage behaviour is consistent with the observation that the 'Blackglas' matrix contains free carbon [35], which burns off at temperatures above 400°C , as well as free silicon and SiO_4 and SiC_4 domains [22]. Increasing the pyrolysis temperature significantly increases the amount of

SiC₄ and reduces the amount of less thermally stable SiO₄ [36,37], which tends to oxidise above 850°C. The short term TGA analysis provides a crude measure of thermal stability, and more detailed studies of the longer term thermal stability of these systems would be required before application of these materials.

The fibre-matrix interfacial shear strength in ceramic matrix composites can be affected by both the mechanical strength of the interface and the action of residual stresses [38].

The relative thermal contractions of matrix and fibre, and the observed process-induced cracking between matrix and fibres (Figure 3), indicate that compressive interfacial residual stresses are unlikely. Hence, the measured interfacial shear strengths represent the mechanical strength of the fibre/matrix interface. The fibre pushout tests (Figure 11) show that sample 1, with the lowest process temperature of 850°C, had significantly the lowest interfacial shear strength. The average strength of interfaces in sample 2, processed at 950°C, was slightly higher than samples 3 and 4, which had the same final process temperature of 1050°C and presented the same average shear strength. The mechanical properties of the interface microstructure depend on both the PIP temperature and also the sequence of PIP treatments, which affects the development of the matrix as demonstrated by the nano-indentation hardness. The low PIP temperature of 850°C leads to a weak interface; the effects of PIP processes at higher temperatures are more complex but lead to stronger interfaces.

The highest flexural strengths and maximum displacements to failure were measured in sample 1 (Figure 5 and Table 4), which had the lowest processing temperature of 850°C. The flexural failures of specimens from the other samples were similar to each other. All showed a tendency for crack deflection parallel to the fibre plies (Figure 6), consistent with low interfacial shear strength between fibre and matrix, particularly

sample 1 that has the weakest interfaces (Figure 11). This encouraged greater delamination, leading to higher strains to failure, with a consequent increase in the maximum flexural stress.

The effective flexural moduli can be used to monitor the development of mechanical damage, since the development of cracking in brittle materials reduces the elastic modulus [39,40]. The effective flexural moduli that were measured using the sample curvature (Figure 8) are most sensitive to this (Figure 9), but may not provide an absolute measure of the sample stiffness as only surface measurements are used and these might be affected by sample alignment (i.e. non-parallel surfaces). The effective moduli obtained via the load-line displacements would be less sensitive to these factors, but are affected by the assumption that the non-observed support pins were rigid. The effect of this is judged to be small, due to the relatively low stiffness of the small and slender test specimens, hence the effective load-line moduli measured at low load (i.e. no damage) allows the relative moduli of the composites to be compared. This shows the effect of the PIP processing temperature on the effective modulus is small; all samples have similar elastic properties.

The direct measurement of the specimen curvature assumes isotropic homogenous behaviour, which is not strictly correct for a composite material. The analysis only provides an effective modulus for this test geometry, but it allows a quite sensitive assessment of relative changes in the effective modulus (Figure 9c). For the comparison, this is presented as a function of the effective flexural strain, obtained using the load-line displacements and the assumption of simple beam theory. Samples 1 and 2 show a significant decrease (up to 33%) with increasing tensile strain. Samples 3 and 4 retain their effective modulus up to higher strains before declining similarly, with

sample 4 showing the highest effective modulus. The modulus decline occurs before the observation of delamination, which is only observed above 90% of the failure load (Figure 6). The modulus decline is attributed to propagation of defects from the matrix, which ultimately coalesce to cause delamination at the failure stress. The relative change in effective modulus with increasing load shows that damage occurs below $0.9R\sigma$, but the spatial resolution of strain imaging by DIC was not sensitive enough to observe this damage as discontinuities in the displacement field until significant damage developed at failure (i.e. Figure 6). There is greater delamination exhibited in sample 1, which was processed at the lowest PIP temperature. This has the lowest interfacial shear strength, which encourages fibre pullout and a more graceful failure.

In terms of the design requirements for spring retention, these measurements conducted at ambient temperature indicate that although sample 1 that was PIP processed at 850°C had the highest density and flexural strength, it had lower thermal stability. Samples 3 and 4, processed at the highest PIP temperature of 1050°C had slightly lower density due to increased closed porosity, good resistance to mechanical damage from tensile strain and good thermal stability.

5 Conclusion

Nextel 312 fibre/SiCO matrix ceramic matrix composites have been manufactured using repeated PIP (polymer infiltration and pyrolysis), with pyrolysis at temperatures between 850°C and 1050°C.

All samples had similar microstructures with no consistent effect of process conditions on the fibre or matrix properties, measured by nano-indentation. The porosity is mostly from closed pores and increased with final PIP temperature.

The effective modulus decreases with increasing flexural strain, with greater resistance to mechanical damage at higher PIP temperature. The highest flexural strength was observed in the sample with the lowest PIP temperature. This had the lowest interfacial shear strength, and graceful failure due to increased delamination increased the maximum flexural strain and strength.

Processing at 950°C or above gave good resistance to mechanical damage from tensile strain and good thermal stability.

6 Acknowledgement

The authors acknowledge Cross Manufacturing Company (1938) Ltd. for financial support of the project, and the valuable discussions with Edward Cross and Paul Blanchard. The project was facilitated by Jim Kreher of Lancer Systems who supplied the material. TJP acknowledges the assistance of Nicola Flanagan (University of Oxford) with the thermal analysis. EPSRC Grant EP/M02833X/1 “University of Oxford: experimental equipment upgrade” supported the Xradia Versa 510 microscope and facilities for data analysis and visualization.

7 References

- [1] Ohnabe H, Masaki S, Onozuka M, Miyahara K, Sasa T. Potential application of ceramic matrix composites to aero-engine components. *Compos Part A Appl Sci Manuf* 1999;30:489–96.
- [2] Kaya C, Kaya F, Butler EG, Boccaccini AR, Chawla KK. Development and characterisation of high-density oxide fibre-reinforced oxide ceramic matrix composites with improved mechanical properties. *J Eur Ceram Soc* 2009;29:1631–9.
- [3] Mecholsky Jr JJ. Engineering research needs of advanced ceramics and ceramic-matrix composites. *Am Ceram Soc Bull* 1989;68:367–75.
- [4] More G, Datta A. Ultra High Temperature Resilient Metallic Seal Development for Aero Propulsion and Gas Turbine Applications. 39th AIAA/ASME/SAE/ASEE Jt. Propuls. Conf. Exhib., 2003, p. 4835.
- [5] Stoll E, Mahr P, Krüger H-G, Kern H, Thomas BJC, Boccaccini AR. Fabrication technologies for oxide--oxide ceramic matrix composites based on electrophoretic deposition. *J Eur Ceram Soc* 2006;26:1567–76.
- [6] Ruggles-Wrenn MB, Ozer M. Creep behavior of NextelTM720/alumina-mullite ceramic composite with $\pm 45^\circ$ fiber orientation at 1200°C. *Mater Sci Eng A* 2010;527:5326–34.
- [7] Prewo KM. Fiber-reinforced ceramics: new opportunities for composite materials, *Ceram. Am Ceram Soc Bull* 1989;68:395–400.
- [8] Strife JR, Brennan JJ, Prewo KM. Status of Continuous Fiber-Reinforced Ceramic Matrix Composite Processing Technology. Hoboken, NJ, USA: John

- 466 Wiley and Sons, Inc; 1990.
- 467 [9] Lewis MH, Tye A, Butler EG, Doleman PA. Oxide CMCs: interphase synthesis
468 and novel fibre development. *J Eur Ceram Soc* 2000;20:639–44.
- 469 [10] Warren R, Deng S. Continuous fibre reinforced ceramic composites for very high
470 temperatures. *Silic Ind* 1996;61:99–107.
- 471 [11] Kanka B, Schneider H. Aluminosilicate fiber/mullite matrix composites with
472 favorable high-temperature properties. *J Eur Ceram Soc* 2000;20:619–23.
- 473 [12] Myers P, Narottam P, Bansal and Jacques Lamon (Eds): *Ceramic Matrix*
474 *Composites Materials, Modeling and Technology*. vol. 78. Hoboken, NJ, USA:
475 John Wiley & Sons; 2015.
- 476 [13] Kaya C, Gu X, Al-Dawery I, Butler EG. Microstructural development of woven
477 mullite fibre-reinforced mullite ceramic matrix composites by infiltration
478 processing. *Sci Technol Adv Mater* 2002;3:35.
- 479 [14] Kaya C, He JY, Gu X, Butler EG. Nanostructured ceramic powders by
480 hydrothermal synthesis and their applications. *Microporous Mesoporous Mater*
481 2002;54:37–49.
- 482 [15] Boccaccini AR, Kaya C, Chawla KK. Use of electrophoretic deposition in the
483 processing of fibre reinforced ceramic and glass matrix composites: a review.
484 *Compos Part A Appl Sci Manuf* 2001;32:997–1006.
- 485 [16] Colombo P. *Polymer derived ceramics: from nano-structure to applications*.
486 *Polym. Deriv. Ceram. from nano-structure to Appl.*, DEStech Publications, Inc;
487 2009, p. 169–77.
- 488 [17] Al-Hussien M, Mall S, Calcaterra JR. Fatigue behavior of NextelTM

- 489 312/BlackglasTM ceramic matrix composite with tensile and zero mean load. Adv
490 Compos Mater Off J Japan Soc Compos Mater 2001;10:1–15.
- 491 [18] Makurunje P, Monteverde F, Sigalas I. Self-generating oxidation protective high-
492 temperature glass-ceramic coatings for Cf/C-SiC-TiC-TaC UHTC matrix
493 composites. J Eur Ceram Soc 2017;37:3227–39.
- 494 [19] Konopka K, Boczkowska A, Batorski K, Szafran M, Kurzydłowski KJ.
495 Microstructure and properties of novel ceramic-polymer composites. Mater Lett
496 2004;58:3857–62. <https://doi.org/10.1016/j.matlet.2004.07.025>.
- 497 [20] Lowden RA, James RD, More K. Interfaces and Mechanical Properties of
498 Continuous Fiber-Reinforced Ceramic Composites. Ceram Trans 1990;19:619–
499 30.
- 500 [21] Colombo P, Mera G, Riedel R, Sorarù GD. Polymer-Derived Ceramics: 40 Years
501 of Research and Innovation in Advanced Ceramics. Am Ceram Soc
502 2010;93:1805–37.
- 503 [22] Belardinelli R. Processing and properties of Blackglas (TM) ceramic matrix
504 composites reinforced with Nextel (TM) 312 (BN) fabric. The University of
505 Texas at Arlington, 1996.
- 506 [23] Al-Hussien M, Mall S, Calcaterra JR. Fatigue behavior of NextelTM
507 312/BlackglasTM ceramic matrix composite with tensile and zero mean load. Adv
508 Compos Mater 2001;10:1–15.
- 509 [24] Tiegs T. Ceramic matrix composites: edited by R. Warren; Chapman and Hall;
510 New York; 1992; 272 pp.; ISBN 0-216-92682-3 1993.
- 511 [25] Ghasemi Nejhad MN, Bayliss JK, Yousefpour A. Processing and performance of

512 continuous fiber ceramic composites by preceramic polymer pyrolysis: II - Resin
 513 transfer molding. *J Compos Mater* 2001;35:2239–55.

514 [26] Hussey A, De Meyere R, Deck C, Armstrong DEJ, Zayachuk Y. Statistically
 515 sound application of fiber push-out method for the study of locally non-uniform
 516 interfacial properties of SiC-SiC fiber composites. *J Eur Ceram Soc*
 517 2020;40:1052–6. <https://doi.org/10.1016/j.jeurceramsoc.2019.11.041>.

518 [27] Rahimi S, Engelberg DL, Duff JA, Marrow TJ. In situ observation of
 519 intergranular crack nucleation in a grain boundary controlled austenitic stainless
 520 steel. *J Microsc* 2009;233:423–31. [https://doi.org/10.1111/j.1365-](https://doi.org/10.1111/j.1365-2818.2009.03133.x)
 521 [2818.2009.03133.x](https://doi.org/10.1111/j.1365-2818.2009.03133.x).

522 [28] Duff JA, Marrow TJ. In situ observation of short fatigue crack propagation in
 523 oxygenated water at elevated temperature and pressure. *Corros Sci* 2012;68:34–
 524 43. <https://doi.org/10.1016/j.corsci.2012.10.030>.

525 [29] Cook A, Stevens N, Duff J, Mshelia A, Leung T-S, Lyon S, et al. Atmospheric-
 526 Induced Stress Corrosion Cracking of austenitic stainless steels under limited
 527 chloride supply. 18th Int. Corros. Congr. 2011, vol. 2, Perth, Australia:
 528 International Corrosion Congress; 2011, p. 1438–49.

529 [30] Kovac J, Alaux C, Marrow TJ, Govekar E, Legat A. Correlations of
 530 electrochemical noise, acoustic emission and complementary monitoring
 531 techniques during intergranular stress-corrosion cracking of austenitic stainless
 532 steel. *Corros Sci* 2010;52:2015–25. <https://doi.org/10.1016/j.corsci.2010.02.035>.

533 [31] Eugster SR. Geometric continuum mechanics and induced beam theories. vol. 75,
 534 New York: Springer; 2015, p. 55–81.

- 535 [32] Liang C, Hutchinson JW. Mechanics of the Fiber Push-Out Test. *Mech Mater*
536 1993;14:207–21.
- 537 [33] Colombo P. Polymer derived ceramics: from nano-structure to applications.
538 DEStech Publications, Inc; 2010.
- 539 [34] Cullity BD. Elements of X-ray Diffraction. Addison-Wesley Publishing; 1956.
- 540 [35] Colombo P. The SiCO System. *Polym. Deriv. Ceram. from nano-structure to*
541 *Appl.*, Lancaster: DEStech Publications, Inc; 2009, p. 170–84.
- 542 [36] Hurwitz FI, Meador MAB. Tailoring silicon oxycarbide glasses for oxidative
543 stability. *J Sol-Gel Sci Technol* 1999;14:75–86.
- 544 [37] Kleebe H-J, Gregori G, Babonneau F, Blum YD, MacQueen DB, Masse S.
545 Evolution of C-rich SiOC ceramics: Part I. Characterization by integral
546 spectroscopic techniques: Solid-state NMR and Raman spectroscopy. *Zeitschrift*
547 *Für Met* 2006;97:699–709.
- 548 [38] Goettler RW, Faber KT. Interfacial shear stresses in fiber-reinforced glasses.
549 *Compos Sci Technol* 1990;37:129–47.
- 550 [39] Phani KK, Niyogi SK. Young’s modulus of porous brittle solids. *J Mater Sci*
551 1987;22:257–63. <https://doi.org/10.1007/BF01160581>.
- 552 [40] Marrow TJ, Liu D, Barhli SM, Mora LS, Vertyagina Y, Collins DM, et al. In situ
553 measurement of the strains within a mechanically loaded polygranular graphite.
554 *Carbon N Y* 2016;96:285–302.

555

556

8 Figure Captions

Figure 1: (a) SEM image of the bulk structure of the CMC (sample 1) with inherent defects from matrix cracking and porosity (b) SEM image of the elliptical cross-sections of the fibres embedded in the matrix (c) TEM bright field image of the fibre and the matrix with the BN interface in between (d) a higher resolution lattice image, using objective aperture, of the fibre structure.

Figure 2: X-ray diffraction spectra for the four sample materials.

Figure 3: X-ray computed tomographs, with porosity visualised by image grey-scale segmentation: a) vertical slice across the 0°/90° plies; (b) to (e) show 3D visualisations with threshold segmentation of pores and cracks for samples (1) to (4) respectively.

Figure 4: Thermo-gravimetric analysis (in air), showing relative mass loss with temperature.

Figure 5: Flexural stress vs nominal flexural strain (from cross-head displacement) for three tested specimens of each of the four sample material

Figure 6: Maximum normal surface 3D strain, obtained by digital image correlation (DIC) in flexural bending, at a) 0.9σ and b) σ (i.e. 90% and 100% of the failure stress)

Figure 7: Schematic illustration of the y-z planes between which relative x-displacements were measured using DIC.

Figure 8: The normalized flexural strain (ϵ_x/M) as a function of distance from the beam centre for different loads in example specimens from (a) sample 1 (b) sample 2 (c) sample 3 and (d) sample 4.

578 Figure 9: The effective flexural modulus values obtained using (a) the load-line
579 displacement (b) flexural strain gradient. The effective flexural modulus (strain
580 gradient), relative to that at 20 N, is shown in (c) as a function of the flexural strain
581 (from load-line displacement).

582 Figure 10: Nanoindentation measurements for matrix and fibre: a) modulus and b)
583 hardness (mean and 95% confidence interval). Data are summarised in Table 5.

584 Figure 11: Cumulative frequency for the interfacial shear strengths measured for the
585 four sample materials by fibre pushout.

586

587 **Author Statement**

588 **Talha J. Pirzada:** Conceptualisation, Methodology, Investigation, Formal analysis, ,
589 Writing - Original Draft, Visualization, **Shraddha Singh:** Investigation, **Robin De**
590 **Meyere:** Investigation, **Philip Earp:** Investigation, **Marina Galano:** Supervision,
591 Writing - Review & Editing **T. James Marrow:** Conceptualisation, Supervision,
592 Writing - Review & Editing, Funding acquisition.

593

594 *Table 1: Summary of the manufacturing parameters for the four sample materials*

Sample Number	Manufacturing Parameters
1	6 x PIP at 850°C
2	6 x PIP at 950°C
3	6 x PIP at 1050°C
4	5 x PIP at 950°C then 1 x PIP at 1050°C

595

Table 2: Total observed porosity by threshold segmentation of X-ray tomographs (mean \pm sample standard deviation for 5 measurements) and bulk density		Pore Volume Fraction (%)	Density (specific gravity)
Sample Number			
1		9.4 \pm 0.9	2.35 \pm 0.19
2		11.2 \pm 1.1	2.30 \pm 0.18
3		15.2 \pm 1.4	2.19 \pm 0.18
4		14.6 \pm 1.2	2.21 \pm 0.18

596

597 *Table 3: Mass change up to 900°C (%): the total mass and mass loss in ranges of i) up*
 598 *to 300°C; ii) between 300° and 600°C;and iii) between 600°C and 900°C. The*
 599 *measurement uncertainty is 0.05%.*

Sample Number	Total %	up to 300°C	300-600°C	600-900°C
1	6.5	2.6	1.4	2.7
2	4.5	2.2	0.7	1.4
3	4.5	1.5	1.7	1.4
4	4.0	1.5	0.9	1.6

600

Table 4: Flexural strengths and effective flexural moduli (using cross-head displacement between 0.1% and 0.2% strain) obtained from three-point bend testing (mean \pm maximum deviation from the mean of 3 measurements). The effective flexural elastic moduli are also obtained from the strain gradient (mean \pm standard error) and load-line displacement (mean \pm maximum deviation from mean) at 20 N (\sim 18 MPa) and 60 N (\sim 54 MPa) load.

Sample Number	Flexural Strength (MPa)	Effective Flexural Modulus (GPa) (cross-head)	Effective Flexural Modulus) (GPa) (strain gradient)		Effective Flexural Modulus) (GPa) (load-line)	
			20 N	60 N	20 N	60 N
1	70.9 \pm 3.6	22.0 \pm 1.2	27.3 \pm 1.6	20.4 \pm 0.4	29.2 \pm 1.6	23.3 \pm 0.6
2	55.2 \pm 2.4	22.2 \pm 0.8	31.4 \pm 1.6	24.5 \pm 0.4	30.8 \pm 1.7	25.6 \pm 0.7
3	56.5 \pm 3.2	23.7 \pm 1.3	33.4 \pm 1.8	31.8 \pm 0.6	33.6 \pm 1.8	34.1 \pm 0.9
4	60.3 \pm 3.1	23.8 \pm 2.5	26.6 \pm 1.4	24.9 \pm 0.4	27.9 \pm 1.6	26.3 \pm 0.7

Table 5: Fibre and matrix modulus and hardness, measured by nanoindentation (sample mean \pm 95% confidence interval [n measurements]).

Sample Number	Hardness (MPa)		Modulus (GPa)	
	Fibre	Matrix	Fibre	Matrix
1	10.8 \pm 1.1 [18]	7.1 \pm 0.5 [24]	142.6 \pm 11.6 [18]	116.0 \pm 4.9 [24]
2	10.1 \pm 1.1 [21]	7.2 \pm 1.3 [24]	123.8 \pm 12.2 [21]	101.1 \pm 9.6 [24]
3	9.5 \pm 0.8 [23]	7.2 \pm 0.9 [14]	132.8 \pm 10.8 [23]	112.0 \pm 12.4 [14]
4	9.2 \pm 1.3 [20]	5.7 \pm 0.2 [10]	140.0 \pm 10.6 [20]	99.6 \pm 3.5 [10]

613 *Table 6: Interfacial shear stress (mean \pm sample standard deviation) obtained by fibre*
614 *pushout testing [n measurements].*

Sample Number	Interfacial Shear Stress (MPa)
1	31.4 \pm 18.3 [48]
2	67.6 \pm 22.1 [35]
3	53.2 \pm 20.3 [42]
4	56.2 \pm 26.2 [200]

615

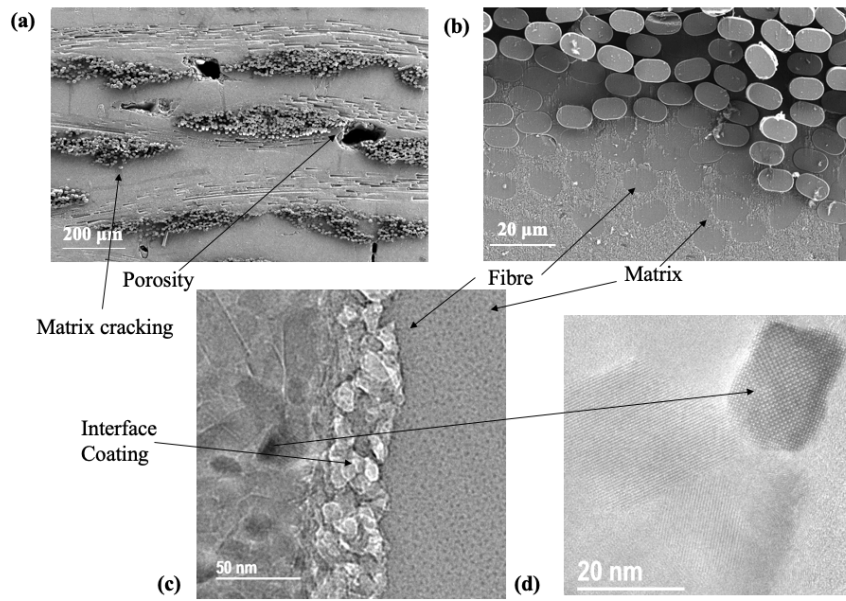


Figure 1: (a) SEM image of the bulk structure of the CMC (sample 1) with inherent defects from matrix cracking and porosity (b) SEM image of the elliptical cross-sections of the fibres embedded in the matrix (c) TEM bright field image of the fibre and the matrix with the BN interface in between (d) a higher resolution lattice image, using objective aperture, of the fibre structure.

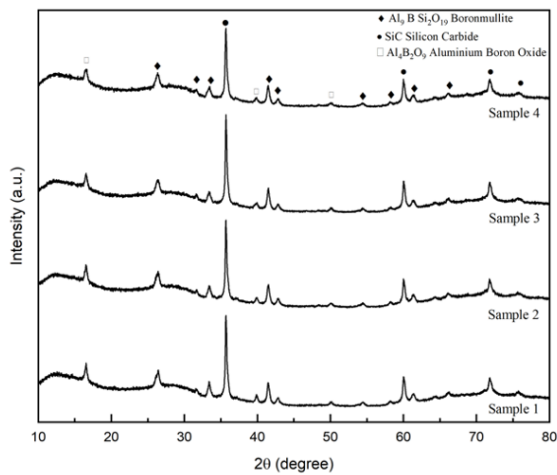


Figure 2: X-ray diffraction spectra for the four sample materials.

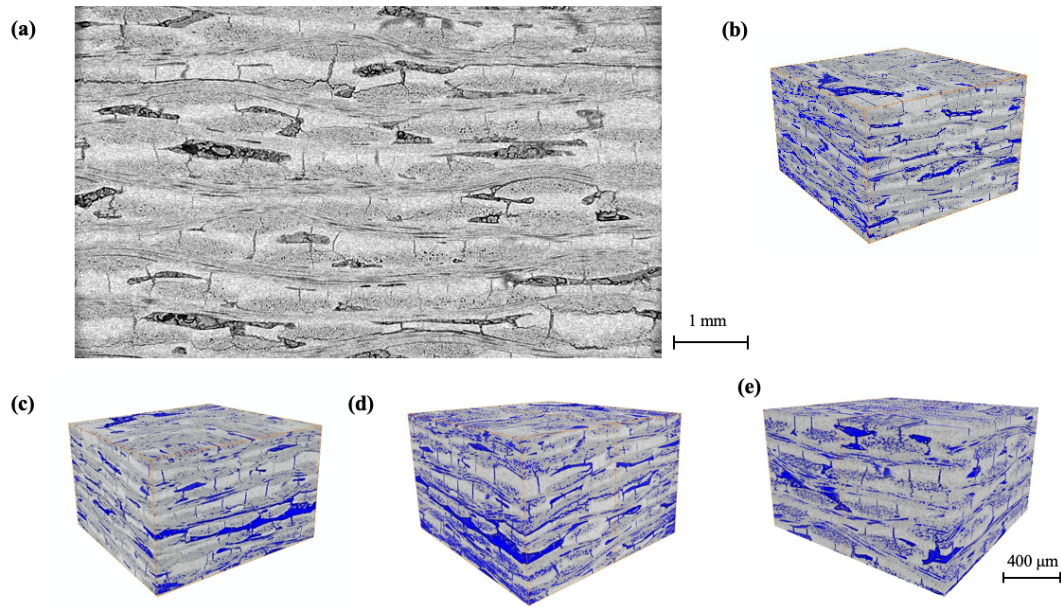


Figure 3: X-ray computed tomographs, with porosity visualised by image grey-scale segmentation: a) vertical slice across the $0^\circ/90^\circ$ plies; (b) to (e) show 3D visualisations with threshold segmentation of pores and cracks for samples (1) to (4) respectively.

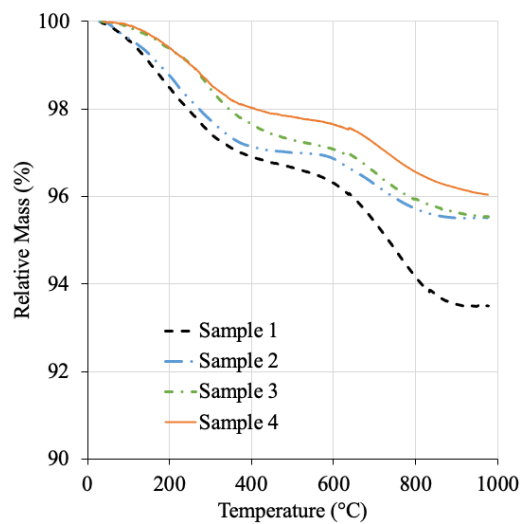


Figure 4: Thermo-gravimetric analysis (in air), showing relative mass loss with temperature.

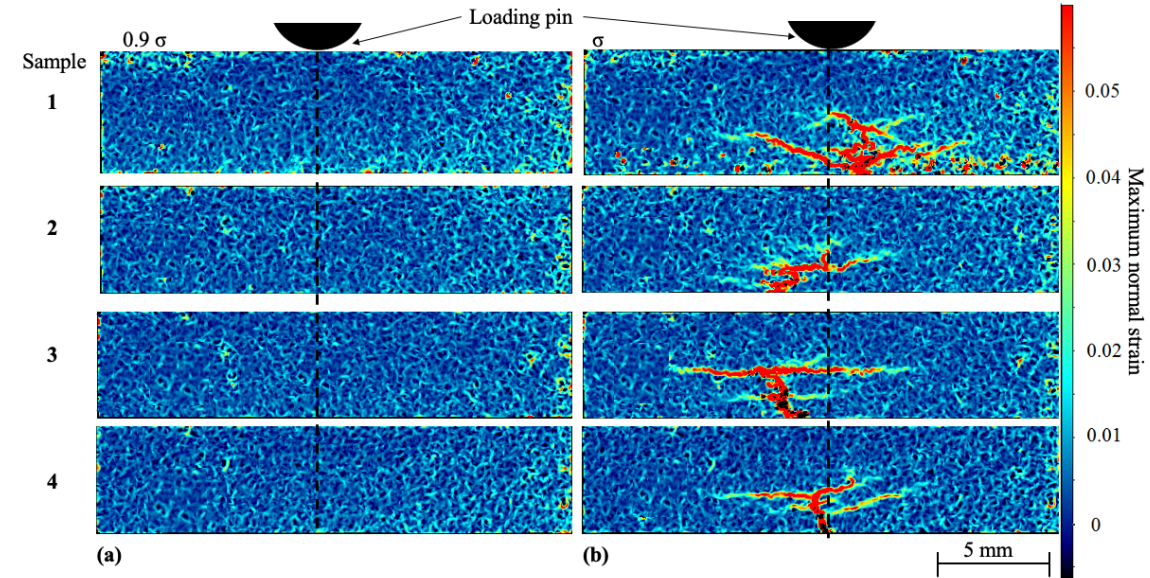
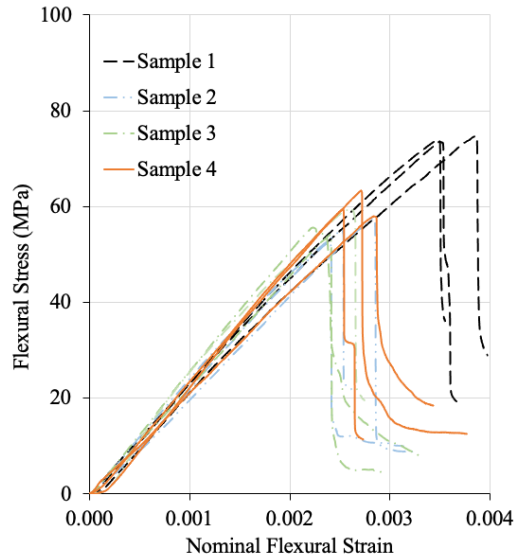


Figure 6: Maximum normal surface 3D strain, obtained by digital image correlation (DIC) in flexural bending, at a) 0.9σ and b) σ (i.e. 90% and 100% of the failure stress)

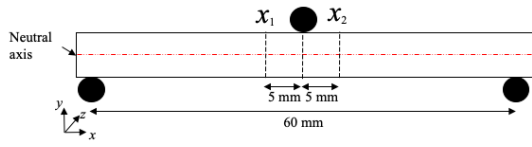


Figure 7: Schematic illustration of the y-z planes between which relative x-displacements were measured using DIC.

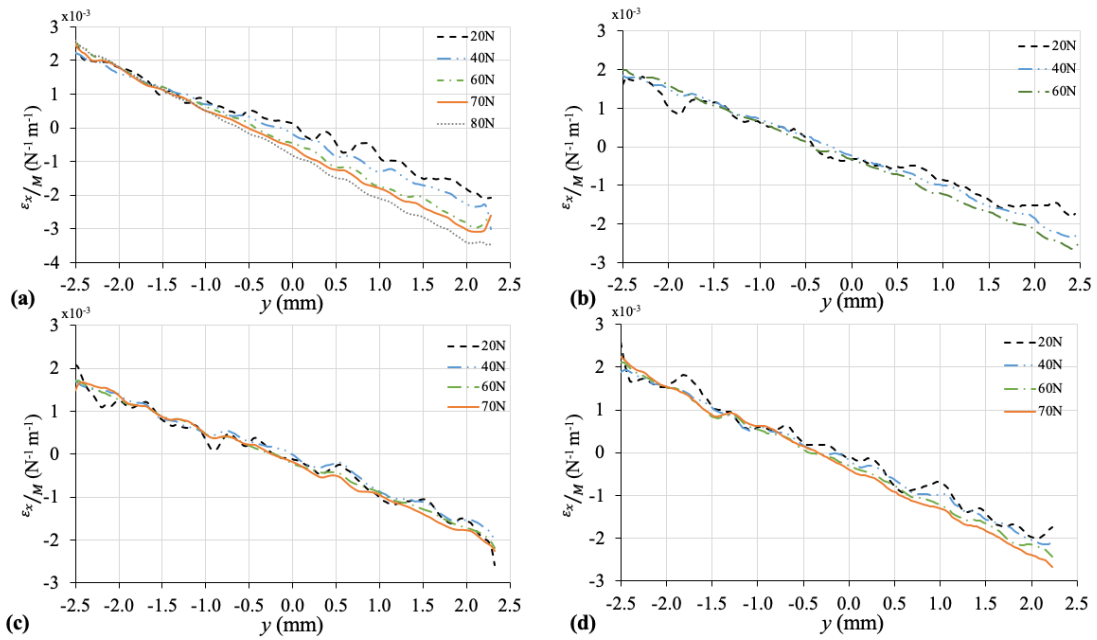


Figure 8: The normalized flexural strain (ϵ_x/M) as a function of distance from the beam centre for different loads in example specimens from (a) sample 1 (b) sample 2 (c) sample 3 and (d) sample 4.

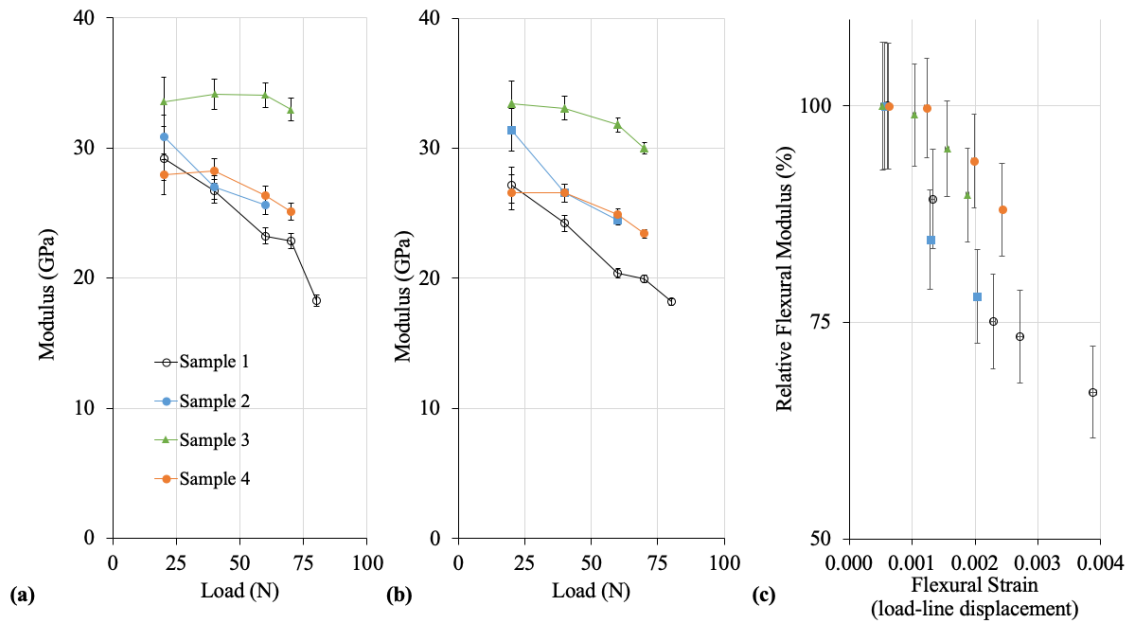


Figure 9: The effective flexural modulus values obtained using (a) the load-line displacement (b) flexural strain gradient. The effective flexural modulus (strain gradient), relative to that at 20 N, is shown in (c) as a function of the flexural strain (from load-line displacement).

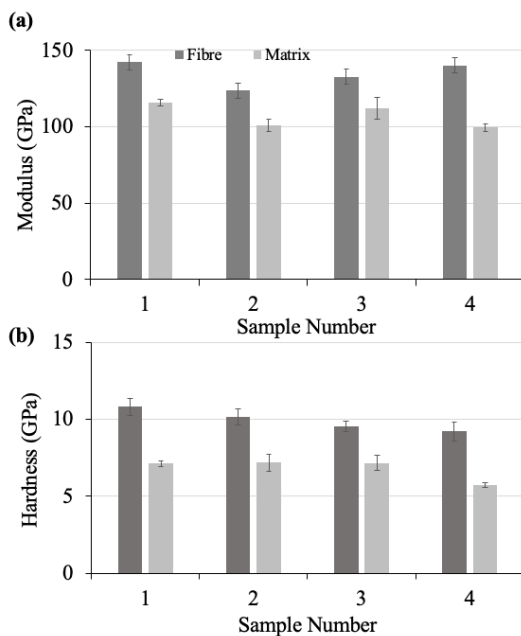
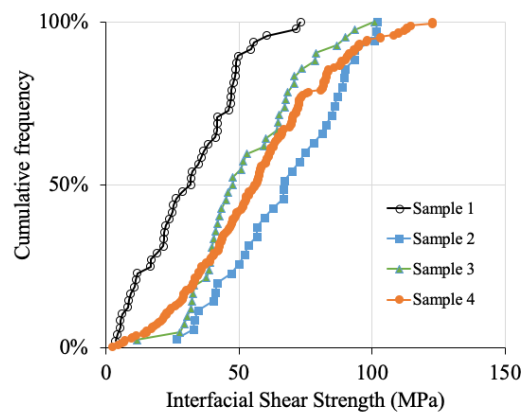


Figure 10: Nanoindentation measurements for matrix and fibre: a) modulus and b) hardness (mean and 95% confidence interval). Data are summarised in Table 5.



652

653 *Figure 11: Cumulative frequency for the interfacial shear strengths measured for the*
 654 *four sample materials by fibre pushout. Mean values summarised in Table 6.*